
Effective Viscous Damping Enables Morphological Computation in Legged Locomotion

An Mo¹, Fabio Izzi^{1,2} Daniel F. B. Haeufle² and Alexander Badri-Spröwitz^{1,*}

¹*Dynamic Locomotion Group, Max Planck Institute for Intelligent Systems, Stuttgart, Germany*

²*Hertie-Institute for Clinical Brain Research, University of Tübingen, Tübingen, Germany*

Correspondence*:
Alexander Badri-Spröwitz
sprowitz@is.mpg.de

ABSTRACT

Muscle models and animal observations suggest that physical damping is beneficial for stabilization. Still, only a few implementations of mechanical damping exist in compliant robotic legged locomotion. It remains unclear how physical damping can be exploited for locomotion tasks, while its advantages as sensor-free, adaptive force- and negative work-producing actuators are promising. In a simplified numerical leg model, we studied the energy dissipation from viscous and Coulomb damping during vertical drops with ground-level perturbations. A parallel spring-damper is engaged between touch-down and mid-stance, and its damper auto-disengages during mid-stance and takeoff. Our simulations indicate that an adjustable and viscous damper is desired. In hardware we explored effective viscous damping and adjustability and quantified the dissipated energy. We tested two mechanical, leg-mounted damping mechanisms; a commercial hydraulic damper, and a custom-made pneumatic damper. The pneumatic damper exploits a rolling diaphragm with an adjustable orifice, minimizing Coulomb damping effects while permitting adjustable resistance. Experimental results show that the leg-mounted, hydraulic damper exhibits the most effective viscous damping. Adjusting the orifice setting did not result in substantial changes of dissipated energy per drop, unlike adjusting damping parameters in the numerical model. Consequently, we also emphasize the importance of characterizing physical dampers during real legged impacts to evaluate their effectiveness for compliant legged locomotion.

Keywords: damping, energy dissipation, legged locomotion, ground disturbance, drop test, rolling diaphragm

1 INTRODUCTION

While less understood, damping likely plays an essential role in animal legged locomotion. Intrinsic damping forces can potentially increase the necessary force output during unexpected impacts (Müller et al., 2014), stabilize movements (Shen and Seipel, 2012; Kalveram et al., 2012; Secer and Saranli, 2013; Abraham et al., 2015), and reject unexpected perturbations (Haeufle et al., 2010; Kalveram et al., 2012), e.g., sudden variations in the ground level (Figure 1). Stiffness in comparison has been studied extensively in legged locomotion. Its benefits have been shown both in numerical simulations, e.g., through spring-loaded

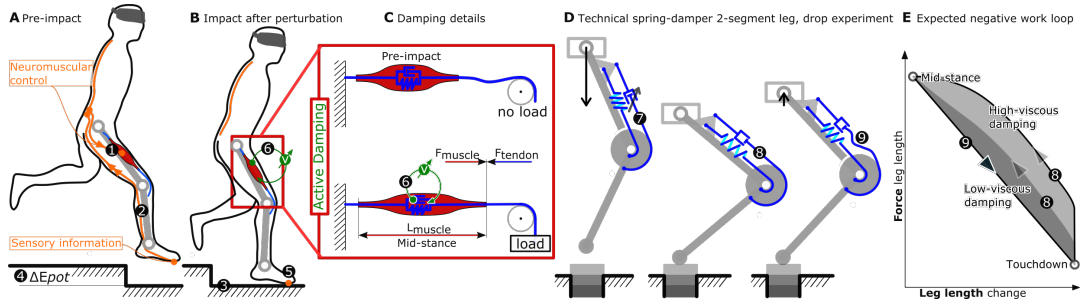


Figure 1. (A-C) Problem identification, and related research question. The limited **nerve conduction velocity in organic tissue** (More et al., 2010) ② presents a significant hazard in legged locomotion. **Local neuromuscular strategies** ⑥ provide an **alternative means** of **timely and tunable force and power production**. Actuators like the indicated **knee extensor muscle** keep the leg extended during stance phase (muscle length L_{muscle}), by producing the appropriate amount of muscle force (F_{muscle}), correctly **timed**. **Neuromuscular control** ① plays a major role initiating and producing these active muscle forces, but works best only during unperturbed locomotion. **Sensor information** from foot contact travels via **nerves bundles** ② to the spinal cord, but with **significant time delays** in the range of $t = 40$ ms (More and Donelan, 2018, for 1 m leg length) and more. Hence, the locomotion control system can become ‘**sensor blind**’ due to **conduction delays, for half a stance phase**, and can miss unexpected perturbations like the depicted step-down. During step-down perturbations ③ additional energy ④ is inserted into the system. Viscous damper-like mechanisms **produce velocity dependent counter-forces, and can dissipate kinetic energy**. **Local neuromuscular strategies** ⑥ producing tunable, viscous damping forces would **act instantaneously and adaptively**. Such strategies ⑥ could also be robust to uncontrolled and harsh impacts of the foot after perturbations ⑤, better than **sensor-based strategies**. In this work (D) we are testing and characterizing spring-damper configurations mounted to a two-segment leg structure, during rapid- and slow-drop experiments, for their feasibility to **physically** and instantaneously produce tunable, speed-dependent forces extending the leg. Work loops (E) will indicate how much effective negative work is dissipated, between touch-down and mid-stance, and mid-stance and takeoff. Prior to impact ⑦ and during the leg loading ⑧ the spring-damper’s tendons act equally. Starting at mid-stance, the main spring extends the knee leading to leg extension, leaving the damper’s tendon slack ⑨ until it recovered.

inverted pendulum (SLIP) models (Mochon and McMahon, 1980; Blickhan et al., 2007), and physical implementations (Hutter et al., 2016; Spröwitz et al., 2013; Ruppert and Badri-Spröwitz, 2019).

What combines both mechanical stiffness and intrinsic, mechanical damping is their sensor- and computational-free action. A spring-loaded leg joint starts building up forces exactly at the moment of impact. Mechanical stiffness or damping act instantaneously, and are not subject to delays from post-processing sensor data (Grimminger et al., 2020), delays from limited nerve conductive velocities (More and Donelan, 2018), or uncertainties in the estimation of the exact timing of swing-to-stance switching (Bledt et al., 2018).

Legged robots commonly exploit *virtual damping*; actively produced and sensory-controlled negative work in the actuator (Seok et al., 2015; Hutter et al., 2012; Havoutis et al., 2013; Kalouche, 2017; Grimminger et al., 2020). Virtual damping requires high-frequency force control, and actuators mechanically and electrically capable of absorbing peaks in negative work. In comparison, mechanical damping based systems (Hu et al., 2019; Garcia et al., 2011) act instantaneously, share impact loads with the actuator when in parallel configuration, and remove the need for sensing and control feedback. Hence, physical damping has the potential to contribute to the *morphological computation* (Zahedi and Ay, 2013; Ghazi-Zahedi et al., 2016) of a legged system.

Energy dissipation can be achieved by different damping principles, e.g., viscous damping, and Coulomb damping. Viscous damping reacts to a system motion with a force that is linearly or non-linearly proportional to the system-damper relative velocity. Coulomb damping generates a constant force (Serafin, 2004). From a simple control perspective viscous damping can be beneficial for the negotiation of perturbations in locomotion as it approximates the characteristics of a differential, velocity-dependent term. Yet it is unknown how this intuition transfers into reality where real impact dynamics and non-linearities due to the leg geometry alter the stance-phase dynamics of locomotion. It is therefore unclear how real physical damping could be exploited in legged locomotion, and which requirements a damper must fulfill.

In this project, we investigate the effect of damping. We focus on the first half of the stance phase of a vertical drop-down, between touch-down (impact) and mid-stance. We chose the simplified drop-down scenario as it captures the core aspects of more complex, rough-terrain locomotion tasks: negotiating ground contacts that include uncertainties. Our goal is to study the effectiveness of mechanical damping on the leg-system total energy dissipation within one drop cycle (touch-down to lift-off), by quantifying the **effective dissipated energy** $E_{\text{effective}}$. We combine insights from numerical simulations and hardware experiments (Figure 2). By studying the response of two damping strategies (viscous and Coulomb damping) in numerical drop-down simulations, we investigate how damping can influence the dynamics of the impact phase. We then examine how these theoretical predictions relate to hardware experiments with two functionally different, mechanical dampers. Hence we explore and characterize the physical damper implementations in a robot leg for their effectiveness in drop-impacts.

2 NUMERICAL SIMULATION

We use numerical simulations to theoretically investigate the energy dissipation in a leg drop scenario (Figure 2). We compare viscous vs. Coulomb damping to investigate which of the two theoretical concepts may be more suited for the rejection of ground-level perturbations. Also, we investigate how the adjustment of the damping characteristics influences the dissipated energy.

2.1 Model

Based on the core characteristics of the hardware prototype (see below), we implemented a 2-segment leg model with a passive spring-damper element at the (knee-)joint (Figure 3a). This numerical model is a modified version of the 2-segment leg proposed in Rummel and Seyfarth (2008) with an additional damper inserted in parallel to the spring. As a result, our system is non-conservative and would require an active energy supply to maintain stable hopping. However, we here simplify the numerical experimental conditions to a passive vertical drop test. The equation describing our leg dynamics is:

$$\ddot{y}(t) = \frac{F_{leg}(t)}{m} - g \quad (1)$$

where g is the gravitational acceleration, m is the leg mass (lumped at the hip), and $y(t)$ is the time-dependent vertical position from the ground. $F_{leg}(t)$ is the force transmitted to the hip mass - and the ground - through the leg structure. As such, the force depends on the current phase of the hopping cycle:

$$F_{leg}(t) = \begin{cases} 0 & , \text{flight phase: } y(t) > l_0 \\ \frac{y(t)}{\lambda_1 \lambda_2} \frac{\tau(t)}{\sin(\beta(t))} & , \text{ground contact: } y(t) \leq l_0 \end{cases} \quad (2)$$

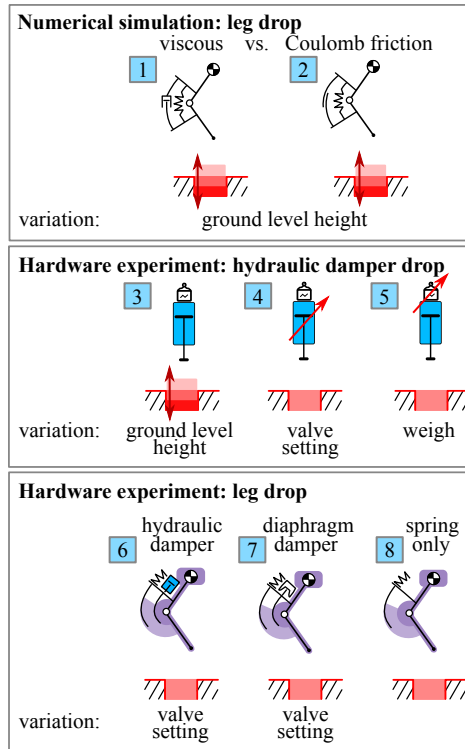


Figure 2. Overview: We study the *effective dissipated energy* $E_{\text{effective}}$ in drop experiments, i.e., the energy dissipation within one drop cycle between touch-down and lift-off (Fig. 6). We focus on a system design with a damper and a spring, both acting in parallel on the knee joint (Fig. 1E and Fig. 3). No active motor is considered as it is not relevant for the drop scenario but would be required for continuous hopping. In **numerical simulations**, we quantify the difference in energy dissipation between viscous [1] and Coulomb friction damping for varying ground level heights [2] (Sec. 2 and Fig. 4). The **first set of hardware experiments** characterizes the industrial hydraulic damper. For this, we **drop the isolated damper** (damper only, not mounted in the) on a force sensor and calculate the energy dissipation. We vary the ground level height [3], the valve setting [4] and the drop mass [5], to investigate its dynamic characteristics (Sec. 4.1 and Fig. 7). For the **second set of hardware experiments**, we **drop 2-segment legs with dampers mounted in parallel to knee springs**. We investigate the energy dissipation dynamics of the hydraulic [6] and diaphragm damper [7] by comparing it to a spring-only condition [8], where the damper cable is simply detached (Sec. 4.2 and Fig. 8). We also vary the valve setting on the dampers to test the dynamic adjustability of damping (Sec. 4.3 and Fig. 9).

with segment length λ_i and knee angle $\beta(t)$ (Figure 3a), l_0 is the leg length at impact. $\tau(t)$ is the knee torque which is produced by the parallel spring-damper element, as in

$$\tau(t) = k r_k^2 (\beta(t) - \beta_0) + \tau_d(t) \quad (3)$$

with k and r_k being the spring stiffness coefficient and lever arm, respectively. $\tau_d(t)$ is the damping torque, which is set to zero during leg extension, i.e., the damper is only active from impact to mid-stance:

$$\tau_d(t) = 0 \quad \text{if } \dot{\beta}(t) > 0 \quad (4)$$

The change in condition reflects the fact that the damper in the mechanical setup (see below) applies forces via a tendon, and the tendon auto-decouples during leg extension. By choosing different definitions of the damper torque $\tau_d(t)$, we can analyse different damper concepts. The model parameters are listed in Table 1.

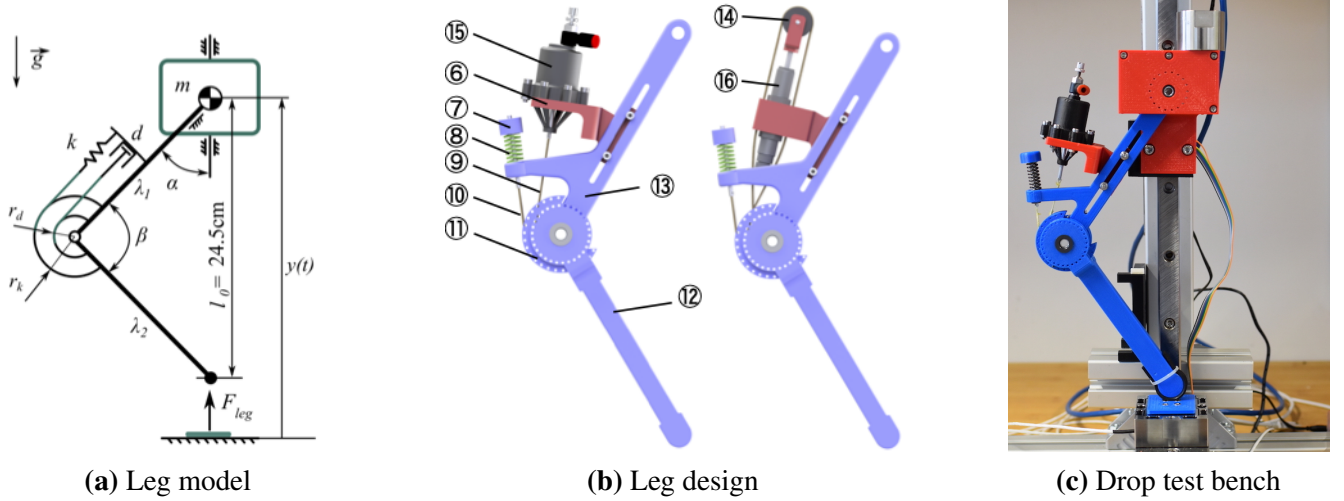


Figure 3. (a) 2-segment spring-damper-loaded leg model used for simulation. (b) Mechanical design of the 2-segment leg. The knee pulley⑪ is fixed with the lower segment⑫, coupled with the spring⑧ and the diaphragm damper⑬ or hydraulic damper⑭ via cables⑨⑩. (c) Drop test bench with 2-segment leg.

Simulations were performed using MATLAB (the MathWorks, Natick, MA) with ODE45 solver (absolute and relative tolerance of 10^{-5} , max step size of 10^{-5} s). When searching for appropriate settings of the numerical solver, we progressively reduced error tolerances and the maximum step size until convergence of the simulation results in Table 2 to the first non-significant digit.

Table 1. Simulation and hardware parameters

Parameters	Symbol	Value	Unit
Mass	m	0.408	kg
Reference drop height	h_0	14	cm
Spring stiffness	k	5900	N/m
Leg segment length	λ_1, λ_2	15	cm
Leg resting length	l_0	24.6	cm
Knee resting angle	β_0	110	deg
Spring lever arm	r_k	2.5	cm
Damper lever arm	r_d	2	cm

2.2 Damping characteristics

We compared two damping concepts in our numerical simulation: (1) *pure* Coulomb friction, i.e., a constant resistance only dependent on motion direction, and *pure* viscous friction, i.e., a damper torque linearly dependent on the knee angular velocity. Accordingly, we tested two different definitions of τ_d :

$$\tau_d(t) = \begin{cases} -d_c r_d \text{sign}(\dot{\beta}(t)) & , \text{ pure Coulomb friction} \\ -d_v r_d^2 \dot{\beta}(t) & , \text{ pure viscous friction} \end{cases} \quad (5)$$

where r_d is the damper level arm, d_c (in N) and d_v (in Ns/m) the Coulomb and viscous friction coefficients, respectively.

2.3 Energy dissipation in numerical drop simulations

With this model, we investigate the difference in energy dissipation in response to step-up/down perturbations (cases [1](#) and [2](#) in Figure 2). For each drop test, the numerically modeled leg starts at rest ($\dot{y}(t) = 0$) with a drop height

$$h = y(t = 0) - l_0 \quad (6)$$

corresponding to the foot clearance at release. The total energy at release is $E_T = mgh$. The energy dissipated in a drop is $E_D = f_{ED}(h, d_{c,v})$ and depends on the drop height and the damping coefficients. Please note that in the following, energies generally depend on the damping parameters. For simplicity, we drop the notation of this dependency.

Equal to the hardware experiments, we use $h_0 = 14$ cm as reference drop height. Its dissipated energy is E_{D_0} and will also depend on the damping parameters. We chose five different desired damping levels (Set 1-5) as a means of scanning a range in which the damping could be adjusted: for each set, the amount of energy that is dissipated at the reference drop height E_{D_0} differs. The chosen E_{D_0} values (Table 2, column ‘‘Reference height’’) correspond to proportional levels ($[0.1, 0.2, \dots, 0.5]$) of the systems potential energy in terms of the leg resting length l_0 , as in

$$E_{D_0} = mg [0.1, 0.2, \dots, 0.5] l_0 \quad (7)$$

This corresponds to damping configurations that dissipate between $\approx 17\%$ and $\approx 88\%$ of the system’s initial potential energy ($E_{T_0} = mgh_0 = 560$ mJ) at the reference height (Table 2, column ‘‘Reference height’’). To achieve these desired damping levels, we adjusted the damper parameters d_c and d_v accordingly (Table 2, column ‘‘Damping coeff.’’). For Set 3, both damping values were adjusted such that at the reference height h_0 both dampers dissipate $E_{D_0} = mg0.3l_0 = 295$ mJ corresponding to 53 % of the total energy E_{T_0} .

In the numerical simulations, we focus on the relation between a ground level perturbation Δh and the change in energy dissipation – and their dependency on the damper characteristics. A drop from a height larger than h_0 corresponds to a step-down ($\Delta h > 0$), and a drop from a height smaller than h_0 to a step-up ($\Delta h < 0$). Each condition introduces a change of the total energy of $\Delta E_T = mg\Delta h$. The change in energy dissipation due to the perturbation is defined as

$$\Delta E_D(\Delta h) = E_D(h_0 + \Delta h) - E_{D_0} \quad (8)$$

which is the difference between the dissipated energy when released from a perturbed height and the dissipated energy when released from the reference height. As a reference, we further define the *full rejection* case where

$$\Delta E_D(\Delta h) = \Delta E_T = mg\Delta h \quad (9)$$

Fully rejecting a perturbation, and within a single drop, comes at the cost of high damping values. In human hopping a full recovery is not seen during experimental drop down perturbations. Instead, a perturbation of $\Delta h = 10\%l_0$ is rejected in two to three hopping cycles (Kalveram et al., 2012, Figs. 2a and 7a). In our results, partial rejections are presented by sets 2 and 3 for $\Delta h = \pm 2.5$ cm.

2.4 Simulation results

Figure 4a shows the relation between the change in drop height and the corresponding change in dissipated energy by the simulated dampers for set 1, 3 and 5 (continuous line for pure viscous friction, dashed for

pure Coulomb friction). For the range of simulated drop heights, pure viscous friction and Coulomb friction dampers change the amount of dissipated energy with an almost linear dependence on the drop height. However, pure viscous friction has a slope closer to the *full rejection* scenario (blue line in Figure 4a), regardless of the set considered. In a step-down perturbation ($\Delta h > 0$ in Figure 4a), pure viscous friction damping dissipates more of the additional energy ΔE_T , while in a step-up perturbation ($\Delta h < 0$) it dissipates less energy than pure Coulomb friction damping. The results show that a viscous damper can reject a step-down perturbation faster, e.g., within less hopping cycles, and it requires smaller correction of the active energy supply during a step-up perturbation.

Adjusting the damping parameters allows to change the reaction to a perturbation (Figure 4). Increasing the damping intensity, i.e., d_v and d_c from set 1 to 5, allows to better match the *full recovery* behaviour (blue line in Figure 4a). However, this comes at the cost of higher energy dissipation already at reference height (Table 2, column ‘reference height’). Increasing damping also affects the energetic advantage of viscous friction damping over Coulomb friction damping (Figure 4b): from set 1 to set 3, the spread between the ΔE_D values of the viscous friction damper and the Coulomb friction damper increases (from 8 mJ to 18 mJ, in Figure 4b). However, negative work slightly reduces with increasing damping rates, e.g., from set 3 to set 5.

Table 2 quantifies the previous findings by indicating the percentage of energy perturbation ΔE_T that each damping approach dissipates when $\Delta h = \pm 2.5$ cm and for all the tested sets of damping coefficients d_v and d_c . The data further confirms the observations from Figure 4, showing that:

1. viscous friction damping outperforms Coulomb friction damping for all the simulated conditions - its dissipated energy is always the closest to 100 % of ΔE_T , which means the closest to *full rejection*;
2. the energetic benefit of viscous friction over Coulomb friction damping, i.e., the spread in percentage values of $\Delta E_D/\Delta E_T$, does not monotonically increase with higher damping rates.

Furthermore, Table 2 shows that for small damping rates, i.e., set 1, viscous friction damping introduces only marginal benefits in energy management compared to Coulomb friction damping: $< 10\%$ spread between the corresponding $\Delta E_D/\Delta E_T$ values.

Table 2. Numerical simulation - Total dissipated energy (E_D) in one drop cycle for different drop heights (h). *Reference height* is the reference drop height $h_0 = 14$ cm. During *step up(down)* condition, the drop height is reduced(increased) by $\Delta h = 2.5$ cm. Percentage values indicate the change in dissipated energy (ΔE_D) relative to the change in system total energy (ΔE_T) due to the height perturbations. Each set simulates two separate mechanical dampers (pure viscous or pure Coulomb friction damping), with damping coefficients chosen to dissipate the same energy (E_{D_0}) at the reference condition. Results of Set 1, 3 and 5 are further described in Fig. 4. For all tested conditions, viscous friction damping outperforms Coulomb friction damping, as indicated by the always higher percentage values.

		Damping coeff.		Step up	Reference height	Step down
		d_v	d_c	$h = h_0 - \Delta h = 11.5$ cm E_D ($\Delta E_D/\Delta E_T$)	$h = h_0 = 14$ cm E_{D_0} (E_{D_0}/E_{T_0})	$h = h_0 + \Delta h = 16.5$ cm E_D ($\Delta E_D/\Delta E_T$)
Set 1	Viscous	29.5 Ns/m	0 N	82 mJ (15%)	97 mJ (17%)	112 mJ (15%)
	Coulomb	0 Ns/m	7.7 N	88 mJ (9%)	97 mJ (17%)	104 mJ (7%)
Set 2	Viscous	68 Ns/m	0 N	167 mJ (30%)	197 mJ (35%)	227 mJ (30%)
	Coulomb	0 Ns/m	17.3 N	178 mJ (19%)	197 mJ (35%)	214 mJ (17%)
Set 3	Viscous	119.4 Ns/m	0 N	249 mJ (46%)	295 mJ (53%)	341 mJ (46%)
	Coulomb	0 Ns/m	29.3 N	264 mJ (31%)	295 mJ (53%)	323 mJ (28%)
Set 4	Viscous	197.1 Ns/m	0 N	330 mJ (63%)	393 mJ (70%)	455 mJ (62%)
	Coulomb	0 Ns/m	46.1 N	346 mJ (47%)	393 mJ (70%)	436 mJ (43%)
Set 5	Viscous	349.4 Ns/m	0 N	411 mJ (81%)	492 mJ (88%)	572 mJ (80%)
	Coulomb	0 Ns/m	76.3 N	423 mJ (69%)	492 mJ (88%)	556 mJ (64%)

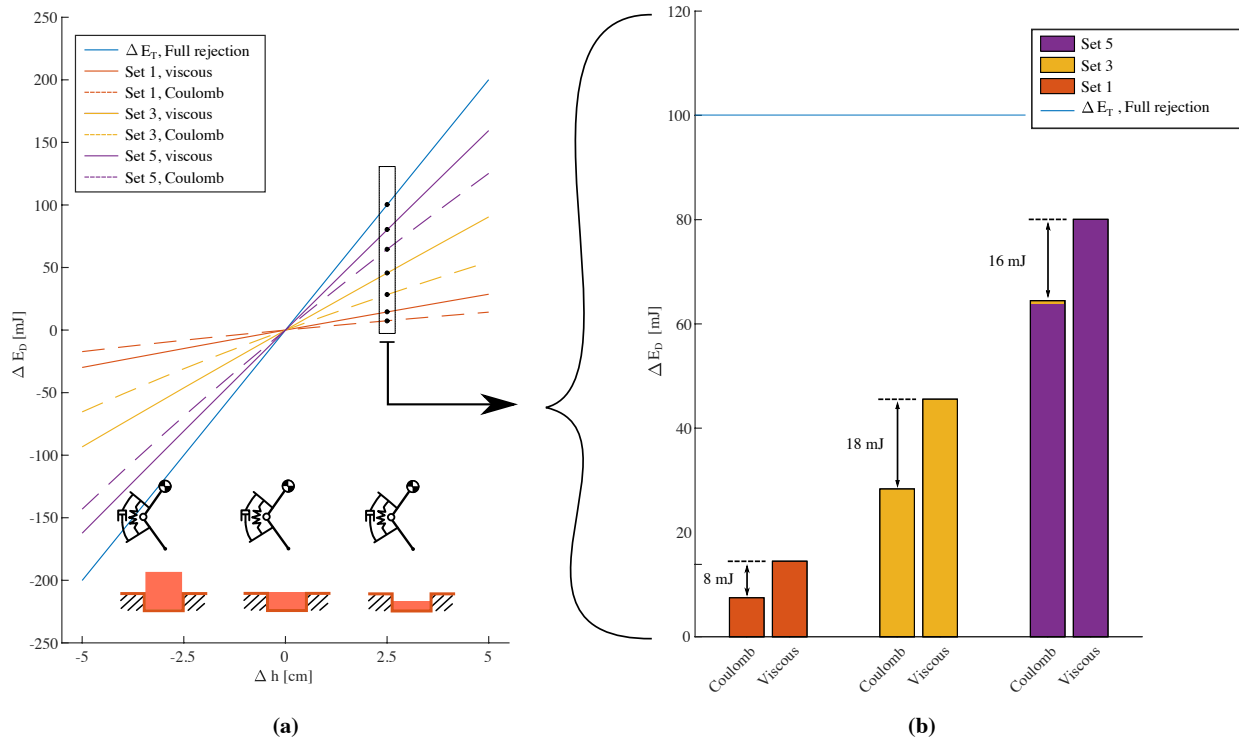


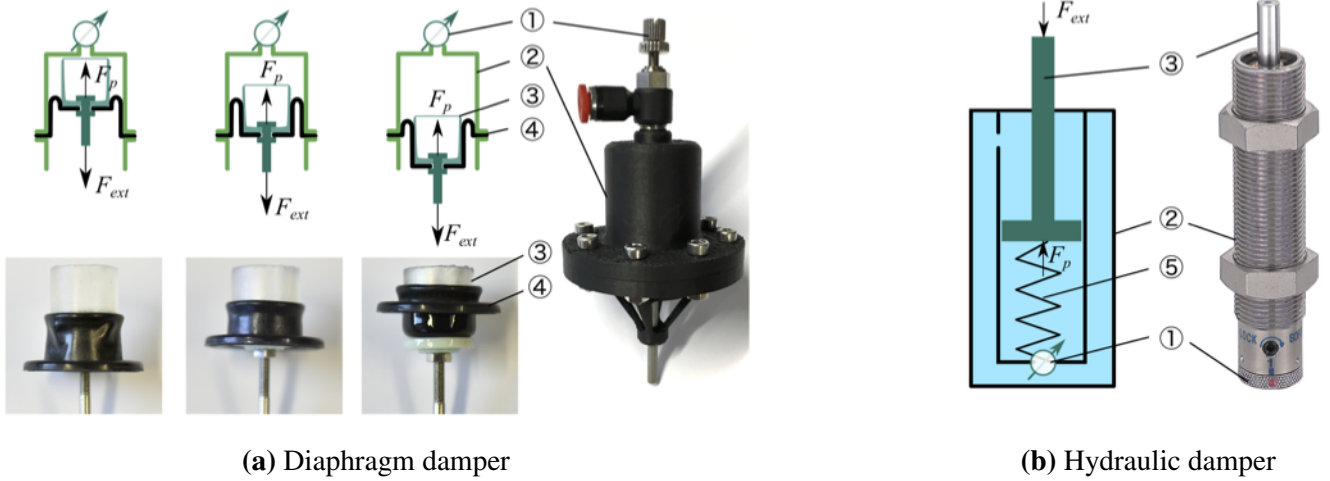
Figure 4. Numerical simulation - (Cases 1 and 2 from Fig. 2) **(a)**: Change of total energy vs. change of drop height for set 1, 3 and 5, with damping coefficients as in Table 2. Continuous lines are viscous damping results, dashed Coulomb damping. Positive perturbations, i.e., $\Delta h > 0$, correspond to step-down perturbations; step-up perturbations, otherwise. The steepest line indicates the slope needed for a *full rejection* of a Δh deviation. Within each set, viscous damping trends match closer the desired *full rejection* behaviour than Coulomb damping data. **(b)**: ΔE_T for $\Delta h = 2.5$ cm. The horizontal line indicate the amount of energy to dissipate for *full rejection* of Δh . Energetic advantage of viscous damping over Coulomb damping, as indicated by the spread in the corresponding ΔE_T values, increases from set 1 to 3, and reduces from set 3 to 5.

3 HARDWARE DESCRIPTION

With the previous results from our numerical simulation in mind, we tested two technical implementations (Figure 5) to produce adjustable and viscous mechanical damping. We implemented a 2-segment leg prototype (Figure 3b) and mounted it to a vertical drop test bench to investigate the role of mechanical damping. The drop test bench produces velocity profiles during impact and stance phase similar to continuous hopping and allows us testing effective damping efficiently and repeatable.

3.1 Rolling Diaphragm Damper

The most common designs of viscous dampers are based on hydraulic or pneumatic cylinders (viscous damping) and can offer the possibility of regulating fluid flow by altering the orifice opening (adjustability). These mechanical dampers can display high Coulomb friction, caused by the mechanical design of the sliding seal mechanisms. Typically, the higher the cylinder pressure is, the higher the Coulomb friction exists. Ideally, we wanted to test one mechanical damper concept with the least possible amount of Coulomb friction. Inspired by the low-friction hydrostatic actuators (Whitney et al., 2014, 2016), we designed a low-Coulomb friction damper based on a rolling diaphragm cylinder. Its cylinder is 3D printed from Onyx material. Figure 5a illustrates the folding movement of this rolling diaphragm mounted on a piston. The



(a) Diaphragm damper

(b) Hydraulic damper

Figure 5. (a)-left-top: schematic of a diaphragm damper, illustrating the motion of rolling diaphragm, which includes an adjustable orifice①, a cylinder②, a piston③, and a rolling diaphragm④. (b)-left: schematic of a hydraulic damper, fluid is sealed inside the cylinder② with an recovery spring⑤ to reset the piston③.

rolling diaphragm is made of an elastomer shaped like a top hat that can fold at its rim. When the piston moves out, the diaphragm envelopes the piston. In the ideal implementation, only rolling contact between the diaphragm and the cylinder occurs, and no sliding contact. Hence Coulomb friction between piston and cylinder is minimized. We measured $F_C \approx 0.3\text{N}$ of Coulomb friction for our rolling diaphragm cylinder, at low speed.

Our numerical simulation results promoted viscous and adjustable friction damping for use in vertical leg-drop. By concept, both properties are satisfied by the diaphragm damper with an adjustable valve. When an external load F_{ext} pulls the damper piston (Figure 5a), the fluid inside the cylinder chamber flows through a small orifice, adjustable by diameter. This flow introduces a pressure drop $\Delta P(t)$, whose magnitude depends on the orifice cross-section area A_o and piston speed $v(t)$. As such, for a given cylinder cross section area A_p , the diaphragm damper reacts to an external load F_{ext} by a viscous force $F_p(t)$ due to the pressure drop $\Delta P(t)$:

$$F_p(t) = A_p \Delta P(t) = A_p f(v(t), A_o) \quad (10)$$

We mounted a manually adjustable valve (SPSNN4, MISUMI) to set the orifice size A_o . For practical reasons (weight, leakage, complexity of a closed circuit with two cylinders) we used air in the diaphragm cylinder as the operating fluid, instead of liquid (Whitney et al., 2014, 2016). Air is compressible, and with a fully closed valve the diaphragm cylinder also acts as an air spring. This additional functionality can potentially simplify the overall design. With the pneumatic, rolling diaphragm-based damper implementation, we focused on creating a light-weight, adjustable damper with minimal Coulomb friction, and air as operating fluid.

3.2 Hydraulic Damper

In the second technical implementation we applied an off-the-shelf hydraulic damper (1214H, MISUMI, Figure 5b), i.e., a commercially available solution for adjustable and viscous damping. Tested against other hydraulic commercial dampers, we found this specific model to have the most extensive range of

adjustable viscous damping and the smallest Coulomb friction ($F_C \approx 0.7\text{N}$). Similarly to the diaphragm damper, this hydraulic damper produces viscous damping by the pressure drop at the adjustable orifice. The operating fluid is oil, which is incompressible. Hence, the hydraulic damper should not exhibit compliant behavior. Other than the diaphragm damper, this hydraulic damper produces damping forces when its piston is pushed, not pulled. Its design also includes an internal spring to recover the piston position when unloaded. In sum, the hydraulic damper features high viscous damping, no air-spring effect, and a higher Coulomb friction compared the custom-designed pneumatic diaphragm damper.

3.3 Articulated Leg Design

The characteristics of a viscous friction damper strongly depend on the speed- and force-loading profile imposed at its piston, because of the complex interaction of fluid pressure and compression, viscous friction, and cavitation (Dixon, 2008). We implemented a mechanical leg to test our two mechanical dampers at loading profiles (speed, force) similar to legged hopping and running.

The 2-segmented robot leg (Figure 3b) is designed with a constant spring and damper lever arm, parameters are provided in Table 3. In all experiments with the 2-segmented leg the leg spring provides elastic joint reaction forces. Dampers are swapped in and out in a modular fashion, depending on the experimental settings. The 2-segment leg design parameters are identical to those in our simulation model. A compression spring^⑧ is mounted on the upper leg segment^⑬. When the leg flexes, the spring is charged by a spring cap^⑦ coupled to a cable^⑩ attached to the lower leg. Either damper^⑮^⑯ is fixed on a support^⑥ on the upper segment^⑬. The support^⑥ can be moved within the upper segment^⑬, to adjust the cable^⑨ pretension. Cables^⑨^⑩ link the damper piston^③ and the spring^⑧ to the knee pulley^⑪, which is part of the lower segment^⑫. During the leg flexion, the tensioned cable transmits forces instantly to the spring and damper. Spring and damper forces counteract the knee flexion. During leg extension, the spring releases energy, while the damper is decoupled due to slackness of the cable. We included a hard stop into the knee joint to limit the maximum leg extension, and achieve a fixed leg length at impact. At maximum leg flexion at high leg loading, segments can potentially collide. We ensured not to hit either hard stops during the drop experiments. The leg structure is 3D printed from ABS material, and design parameters are identical to the numerical model (Table 1). The hydraulic damper^⑯ requires a reverse mechanism^⑭, since its piston requires compression to work. The piston of the diaphragm damper^⑮ was directly connected to the knee pulley. The diaphragm damper^⑮ included no recovery spring^⑤, hence we reset the piston position manually after each drop test. In sum, different spring-damper combinations can be tested with the 2-segment leg setup.

3.4 Experimental set-up, data sampling and processing

We implemented an experimental setup for repetitive measurements (Fig. 3c). A drop bench was used to constrain the leg motion to a single vertical degree of freedom, and linear motion. This allowed us to fully instrument the setup (slider position, and vertical ground reaction forces), and ensured repeatable conditions over trials. Adjusting the drop height allowed us setting the touch-down speed. A linear rail (SVR-28, MISUMI) was fixed vertically on a frame. The upper leg segment was hinged to a rail slider. The rail slider was loaded with additional, external weights, simulating different robot masses. We set the initial hip angle α_0 to align the hip and foot vertically. A hard stop ensured that the upper leg kept a minimum angle $\alpha > \alpha_0$.

Table 3. Drop test settings for experiments

<i>Drop test setup</i>	<i>Fig.</i>	<i>Drop height</i> [cm]	<i>Drop weight</i> [g]	<i>Orifice</i> [~]
Damper (1214H)	7a	3, 5, 7	280	b
	7b	5	280	a, b, c
	7c	3	280, 620	b
Damper (1214H, diaphragm) & leg	8a, 8b	14	408	c
	8c	14	408	damper detached
Damper & leg (simulation)	9a, 9b	14	408	a, c
	9c	14	408	viscous, Coulomb
Damper (1214M) & leg	10	14	408	a, b

Three sensors measured the leg dynamics: the body position y , vertical ground reaction force (GRF) and diaphragm cylinder pressure drop ΔP are recorded by a linear encoder (AS5311, AMS), a force sensor (K3D60a, ME, amplified with 9326, Burster) and a pressure sensor (1141, Phidgets Inc.), respectively (Figure 3c). The duration from touch-down to mid-stance is very short, typically $t \leq 100$ ms, and high-frequency data sampling was required. The encoder data was sampled by Raspberry Pi 3B+ with $f = 8$ kHz sampling rate. Force and pressure data were recorded by an Arduino Uno, with a 10-bit internal ADC at 1 kHz sampling rate. A high-speed camera (Miro Lab 110, Phantom) recorded the drop sequence at $f = 1$ kHz sampling rate. We performed ten trials for each test condition. Sensor data was processed with MATLAB (the MathWorks, Natick, MA). Data was smoothed with a moving average filter, with a filter span of 35 samples for encoder data, and 200 samples for force and pressure data. Repeated experiments of the same test condition are summarized as an envelop defined by the average \pm the standard deviation of the filtered signals.

4 HARDWARE EXPERIMENTS AND RESULTS

In the drop experiments, we characterize both the hydraulic and diaphragm dampers, and the 2-segmented springy leg. We chose three orifice settings (labeled as a, b, and c) for each damper, and focus on the effects of viscous friction damping and adjustable dissipation of energy in the hardware setup. Table 3 lists an overview of the drop tests, and its settings (drop height, weight, orifice setting, damper type). Videos of the experiments can be found in the supplementary material, and online ¹.

4.1 Isolated damper drops, evaluation

In this experiment we characterized the hydraulic damper by dropping it under changing conditions of the instrumented drop setup, without mounting it to the 2-segment leg. The experimental setup allows differentiating effects, compared to the 2-segment leg setup, and to emphasize the viscous damper behavior of the off-the-shelf component. We also applied the results to estimate the range of damping rates available with changing orifice settings. The hydraulic damper was directly fixed to the rail slider into the drop bench (Section 3.4). The piston pointed downwards. We measure the vertical ground reaction force to determine the piston force, and we recorded the vertical position of the slider over time, to estimate the piston speed after it touches the force sensor.

Figure 7 shows the force-speed profiles for drop tests with different drop heights (Figure 7a), orifice settings (Figure 7b), and drop loads (Figure 7c). Data lines in Figure 7 should be interpreted from high

¹ <https://youtu.be/8rD9og2h0TQ>

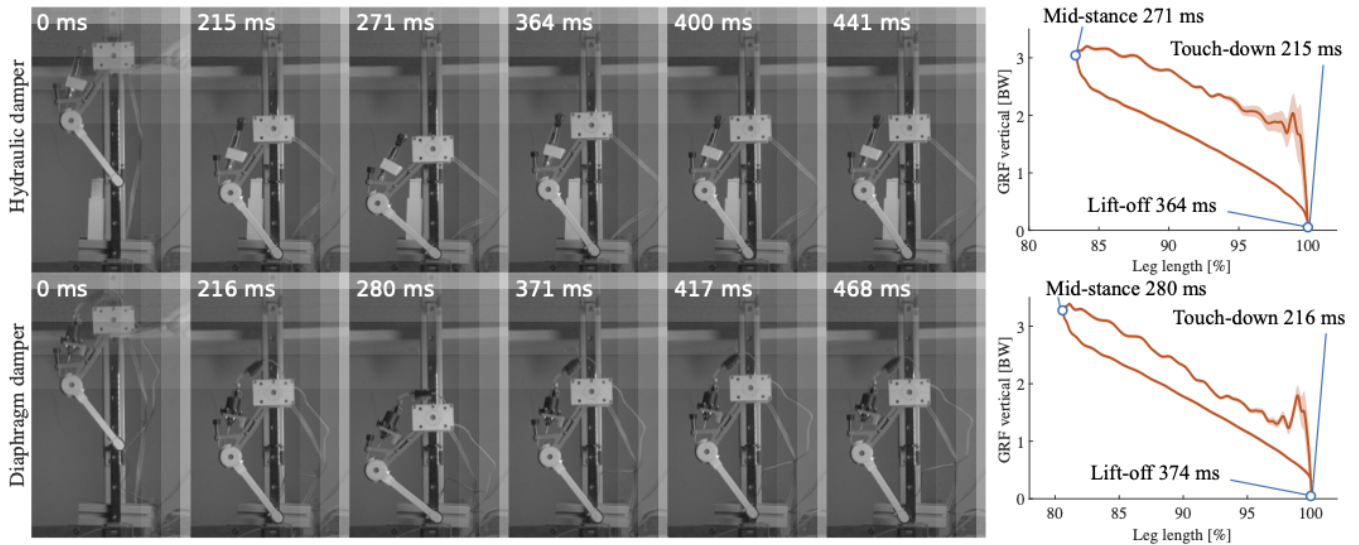


Figure 6. High-speed snapshots of drop experiments starting from release to second touchdown. Leg with hydraulic damper is shown on the top row, leg with diaphragm damper the bottom row. Depicted are from left to right: release, touchdown, mid-stance, lift-off, apex, second touchdown. The right plots illustrate the timing of the events corresponding to the snapshots.

speed (impact, right side of each plot) to low speed (end of settling phase, 0 m/s, left). The time from impact to peak force (right slope of each plot) is (≈ 24 ms), while the negative work (shown in legends) was mainly dissipated along the falling slope in the much longer-lasting settling phase after the peak (left slope of each plot, ≈ 200 ms).

The results from tests with drop heights from 3 cm to 7 cm show viscous damping behavior in the settling phase after peak force (left slope), with higher reaction forces at higher piston speeds with higher dissipation, ranging from 45 N for maximum speeds of 0.6 m/s with 56 mJ to 65 N at 0.9 m/s with 117 mJ. The piston force almost linearly depends on the piston speed (Figure 7a).

Changing the orifice setting at a constant drop height resulted in different settling slopes (Figure 7b). Applying a least-squares fit on the left-falling settling slope, we estimated an adjustable damping rate between 91 Ns/m to 192 Ns/m. The dissipated energy changes in a reverse manner with the orifice settings, from 89 mJ to 81 mJ. Hence adjusting the orifice setting has an effect on the damping rate and the dissipated energy in the isolated hydraulic damper, but not as we intuitively expected.

The rising slope in the impact phase (right part of each curve, Figure 7a, 7b) seems to suggest a reverse linear correlation between the piston force and speed. However, we are interpreting the behaviour as a build-up phase; the hydraulic damper takes time (≈ 24 ms) to build its viscous resistance after the piston impact. Also with heavier weights (620 g (heavy), 280 g (light), Figure 7c), the impact phase equally lasts ≈ 24 ms. After the impact phase with heavy weight, the damper shows the same damping rate (falling slope, left) in the settling phase.

Similar drop tests for the evaluation of the (isolated) diaphragm damper were not possible since the orientation of the internal diaphragm permits only to pull the piston. In the following section we directly test the diaphragm—and the hydraulic—damper on the 2-segment leg structure.

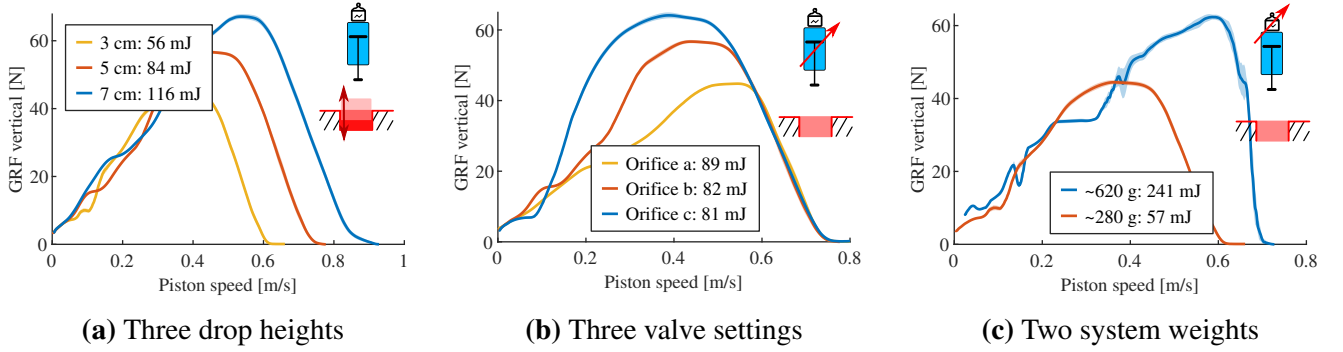


Figure 7. Characterizing the hydraulic damper: a single damper (not leg-mounted) drops onto force sensor. 10 repeated experiments are plotted as an envelop defined by the average $\pm 95\%$ the standard deviation. Reading goes from right to left, i.e. from touch-down at maximum speed to rest (zero). Latter corresponds to the maximum damper compression. **(a)** 280 g drop mass with medium orifice in 3 drop heights. **(b)** 280 g drop mass with 5 cm drop height in 3 orifice settings. **(c)** 3 cm drop height with medium orifice in 2 drop weights.

4.2 Composition of dissipated energy

We performed drop tests of two damper configurations: one off-the-shelf hydraulic damper, and custom-made pneumatic damper, each mounted in parallel to a spring at the 2-segment leg (Section 3.3, Figure 3b), to quantify the effect of viscous friction damping for drop dynamics similar to legged hopping.

For each drop, the effective dissipated energy $E_{\text{effective}}$ was computed by calculating the area enclosed by the vertical GRF-leg length curve from touch-down to lift-off (Josephson, 1985), i.e., the work-loop area. These work-loops are to be read counter-clockwise, with the rising part being the loading during leg flexion, and the falling part being the unloading, due to spring recoil. $E_{\text{effective}}$ does not only consist of the viscous loss E_{viscous} due to the damper, but also Coulomb friction loss in the leg (E_{friction}) and the impact loss E_{impact} due to unsprung masses:

$$E_{\text{effective}} = E_{\text{friction}} + E_{\text{impact}} + E_{\text{viscous}}. \quad (11)$$

We propose a method to indirectly calculate the contribution of viscous friction damping, by measuring and eliminating effects from Coulomb friction, and unsprung masses.

To quantify the Coulomb friction loss E_{friction} , we conducted ‘slow drop’ tests. The mechanical setup is identical to ‘free drops’ test, where the leg is freely dropped from a fixed height. However, in the ‘slow drop’ experiment the 2-segment leg is lowered manually onto the force plat, contacting and pressing the leg-damper-spring system onto the force plate. At slow speed only Coulomb friction in joints and damper act, but no viscous damping or impact losses occur. Consequently the dissipated energy calculated from the size of the work loop is due to Coulomb friction losses E_{friction} .

To identify the impact loss E_{impact} , we remove the viscous component first by detaching the damper cable on the setup. A ‘free drop’ test in this spring only condition measures the contribution of friction loss E_{friction} and impact loss E_{impact} combined. A ‘slow drop’ test of the same setup is able to quantify the friction loss E_{friction} . The impact loss E_{impact} is therefore estimated as the energy difference between ‘free drop’ and ‘slow drop’ in the spring-only condition (Figure 8c). Since the effective dissipated energy $E_{\text{effective}}$ is directly measured, and the friction loss E_{friction} and impact loss E_{impact} are obtained separately, the viscous loss E_{viscous} can be computed according to Eq. 11.

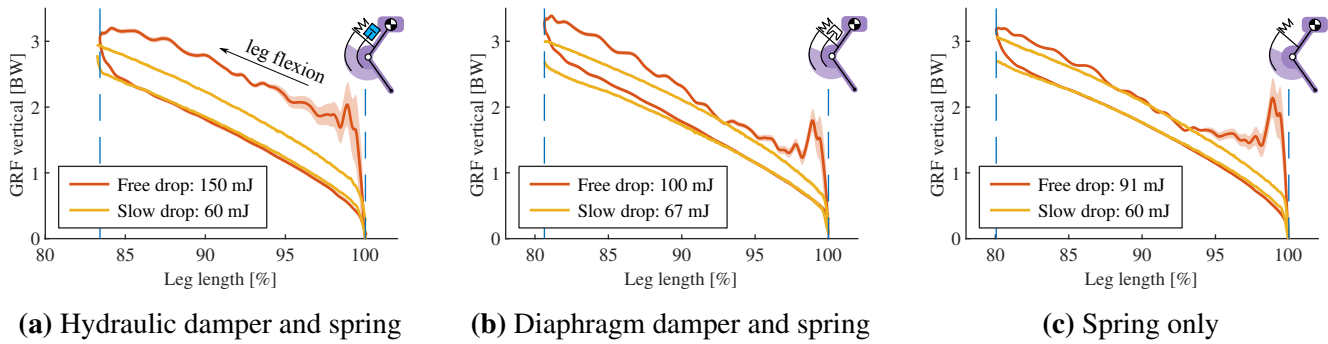


Figure 8. Characterizing the contribution of velocity-dependent damping: Vertical GRF versus leg length change, a 2-DOF leg with damper/spring drops onto the force sensor: Three different hardware configurations were tested, for slow and free drop speeds on the vertical slider. Yellow data lines indicate slow-motion experiments. Experiments ‘start’ bottom right, at normalized leg length 100 %. Reading goes counter-clockwise, i.e. from touch-down to mid-stance is indicated by the upper part of the hysteresis curve, while the lower part indicates elastic spring-rebound, without damper contribution.

Figure 8a, 8b show the ‘free drop’ and ‘slow drop’ results of the hydraulic damper and diaphragm damper, respectively. Both drop heights are 14 cm, at identical orifice setting. We calculated the negative work of each work-loop (range indicated by the two vertical dash lines), as shown in Figure 8. To provide an objective analysis, the work-loop area of each ‘slow drop’ (manual movement) was cut to the maximum leg compression of the corresponding ‘free drop’ condition. The dissipated energy of the leg-mounted hydraulic damper is 150 mJ and 60 mJ for ‘free drop’ and ‘slow drop’, respectively, and 100 mJ and 67 mJ for the diaphragm damper, respectively. According to Figure 8c, the impact loss E_{impact} due to unsprung masses play a large role, accounting for 31 mJ. The viscous loss E_{viscous} of the hydraulic and the diaphragm damper are 59 mJ and 2 mJ, respectively.

4.3 Adjustability of dissipated energy

We tested the adjustability of energy dissipation during leg drops by the altering orifice setting for each leg-mounted damper, and quantified by calculating the size of the resulting work-loops. The drop height was fixed to 14 cm and we used 2 orifice settings. The identical same set-up but in spring-only configuration (damper cables detached) was tested for reference. Work-loop and corresponding effective dissipated energies are illustrated in Figure 9a, 9b. The hydraulic damper-mounted leg dissipated 156 mJ and 150 mJ energy on its two orifice settings, the pneumatic diaphragm damper dissipated 102 mJ and 100 mJ. In Fig 9c, we display results from the numerical model introduced in Section 2 to estimate the work-loop shape that either a pure viscous friction or pure Coulomb friction damper would produce, if dissipating the same amount of energy as the hydraulic damper with orifice-a (Fig 9a). We set the damping coefficients of our numerical model to $E_{D_0} \approx 156$ mJ, so that: $(d_v, d_c) = (51 \text{ Ns/m}, 0 \text{ N})$ for pure viscous friction; and $(d_v, d_c) = (0 \text{ Ns/m}, 13.2 \text{ N})$ for pure Coulomb friction. Work-loops from the numerical simulation differ notably from the experimental data, suggesting that neither the hydraulic or diaphragm damper can easily be approximated as pure viscous or pure Coulomb friction dampers. Both work loops in Figure 9c present about equal amount of dissipated energy. Yet both differ greatly due to their underlying damping dynamics, visible in their unique work-loop shapes. Their individual characteristics are different enough to uniquely identify pure viscous or pure Coulomb friction dampers, from numerical simulation.

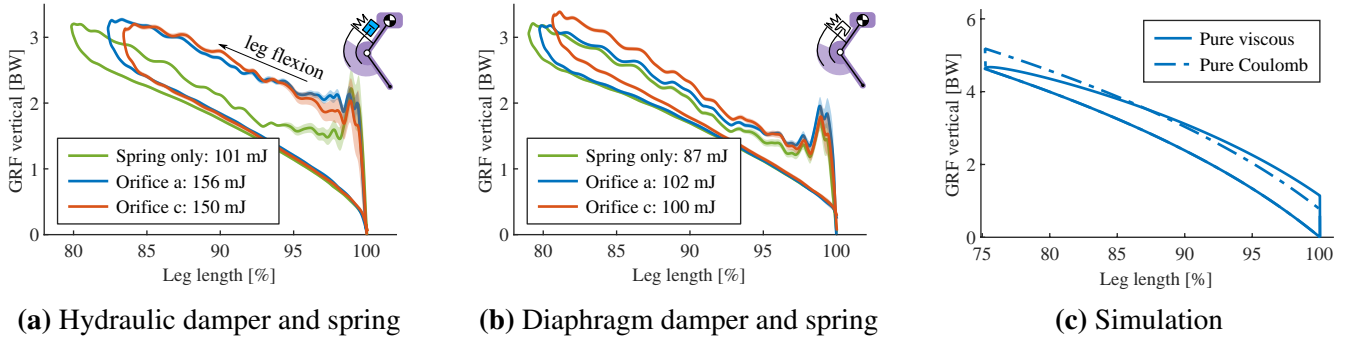


Figure 9. Adjustability/Tunability of damping: Vertical GRF vs leg length change, a 2-DOF leg with damper and spring drops onto the force sensor: Two different hardware configurations were tested, for different orifice settings. **(a) and (b)** show the result from hydraulic damper and diaphragm damper respectively, where the yellow data lines indicate the leg drop without damper for comparison. **(c): Simulated** approximation of hydraulic damper orifice a by a pure viscous and a Coulomb damper. Damping coefficients are chosen to allow same dissipated energy, i.e., $E_{D_0} = 156 \text{ mJ}$: respectively — pure viscous damper: $d_c = 0 \text{ N}$ and $d_v = 51 \text{ Ns/m}$; pure Coulomb damper: $d_c = 13.2 \text{ N}$ and $d_v = 0 \text{ Ns/m}$. None of the two curves can fully capture the work-loop of hydraulic damper.

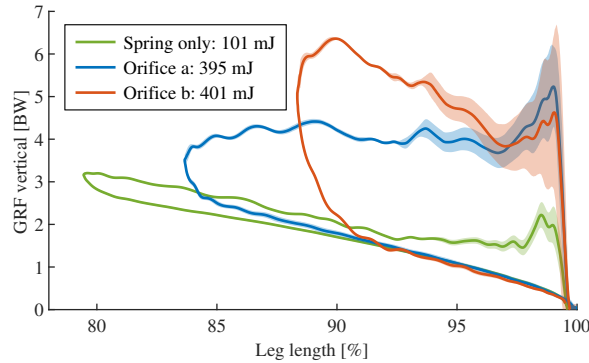


Figure 10. More energy dissipation with another hydraulic damper (1214M): Vertical GRF vs leg length change, a 2-DOF leg with damper and spring drops onto the force sensor: Two orifice settings and one were tested. The result with damper cable detached is also provided as reference.

4.4 Damper selection choices

Results from the previously presented hydraulic damper-1214H showed high effective energy dissipation capabilities: $\approx 27\%$ of the system's total energy (Figure 9a) was dissipated. Depending on the task, other dissipation dynamics are feasible, by selecting appropriate dampers. Here we tested a second hydraulic damper (1210M, MISUMI), under equal hardware experimental conditions compared to damper-1214H. The two applied orifice settings changed the observed work loop both by area and shape (Figure ??). The damper-1210M-spring leg dissipated $\approx 71\%$ of its system's total energy. At selected orifice settings (data not shown here), we recorded over-damped behavior. The over-damped 1210M-spring leg came to an early and complete stop, and without rebound.

5 DISCUSSION

A primary objective of this study was to test how physical dampers could be exploited for locomotion tasks by characterizing multiple available technical solutions. Our numerical model predicted three crucial aspects: (1) a pure viscous friction damper generally performs better than a pure Coulomb friction damper (Figure 4); (2) higher damping rates result in better rejection of ground disturbances (Figure 4a), however

at the cost of higher dissipation at reference height (Table 2); (3) characteristic work loop shapes for pure friction viscous and Coulomb friction damper during leg-drop (Figure 9c). Our hardware findings show that neither of the tested physical dampers approximates as pure viscous or pure Coulomb dampers. The experiments also suggest that the mapping between dissipated energy and damping rates is concealed by the dynamics of the impact and the non-linearity of the force-velocity characteristics of the leg in the stance phase. Therefore, it is vital to test damping in a real leg at impact because the behavior is not merely as expected from the data sheets and the simple model.

Figure 7 characterizes how the hydraulic damper dissipates energy during a free drop. The experimental results show that the dissipated energy of the hydraulic damper scales with drop height (Figure 7a) and weight (Figure 7c), but less intuitively, it reduces with increasing damping rates (Figure 7b). This can be partially interpreted in the context of an ideal viscous damper (as in Eq. (5), just linear) for which the effective dissipated energy $E_{\text{effective}}$ would be calculated as in,

$$E_{\text{effective}} = \int F_p(t) dy_p = \int (d_v \cdot v_p(t)) dy_p \quad (12)$$

where $F_p(t)$ is the damper piston force and y_p is the piston displacement, $v_p(t)$ the corresponding velocity. When increasing the drop height, the velocity at impact is increased, so is $v_p(t)$. With the assumption of Eq. 12, this results in higher damping forces $F_p(t)$, and thus, dissipated energy $E_{\text{effective}}$, as seen in Figure 7a. The heavier drop weight leads to slower deceleration. Therefore the velocity profile $v_p(t)$ is increased, which also leads to higher dissipation $E_{\text{effective}}$ (Figure 7b). An orifice setting of high damping rate will increase the damping coefficient d_v . However, the velocity profile $v_p(t)$ is expected to reduce due to higher resistance. This simple analogy shows that the coupling between damping coefficient d_v and velocity profile $v_p(t)$ makes it difficult to predict the energy dissipation by setting the orifice and serves as an interpretation of why adjusting the orifice generates a relatively small adjustment of 10% (81 mJ-89 mJ) of the dissipated energy. Also, the impact phase (time for the damper to output its designed damping force under sudden load) introduces additional non-linearity to the output force profile. Overall, the results in Figure 7 indicate that we can approximate the damping force produced by the hydraulic damper to be viscous and adjustable— as such dampers are typically designed (Dixon, 2008)—, but the mapping of energy dissipation to orifice setting is difficult to predict in a dynamic scenario. We conclude that characterizing dampers under dynamic load, ideally in the leg design (Figure 6), is necessary.

The work loops of leg drop experiments (Figure 8) show the effects of our tested dampers on a legged system. From touch-down to mid-stance (*leg flexion*), the ‘free drop’ curves show a larger negative work compared to the ‘slow drop’ curves, illustrating that the damper absorbs extra energy. The returning curves (mid-stance to lift-off) of the hydraulic damper aligns well with the ‘slow drop’ curve, indicating the damper is successfully detached due to slackness cable while the spring recoil. Figure 8b shows that the ‘free drop’ force of the diaphragm damper is slightly higher than ‘slow drop’ force in the first half of the leg extension phase. This discrepancy is likely caused by the elastic force component of the diaphragm damper due to sudden expansion of the air chamber volume. The elastic component seems to dominate the damper behavior, which thus acts mostly as an air spring. By separating its energetic components (Eq. 11), we found that the hydraulic damper produces a viscous-like resistance higher than the diaphragm damper (59 mJ versus 2 mJ), indicating the hydraulic damper is more effective in dissipating energy under drop impact. Hence, the hydraulic damper shows more viscous behavior, while the diaphragm damper is more elastic.

Mechanical damping in the system comes at the cost of energy loss, and to maintain periodic hopping, it becomes necessary to replenish E_{D_0} . Therefore, there is a trade-off to consider: simulation results show that higher damping results in faster rejection of ground perturbation at the price of more energy consumption at reference drop height (Table 2, Fig. 4). An adjustable damper would partly address this problem: on level ground, the damping rate could be minimal, and on rough terrain increased. The adjustability of the two dampers is illustrated in Fig. 9a, 9b. We discuss the adjustability from both energy dissipation and dynamic behavior perspectives.

Compared with the spring-only results, both the hydraulic and the diaphragm damper reduced the maximum leg flexion and dissipated more energy. The orifice setting changes the shape of the work loop differently for the two set-ups. For the hydraulic damper (Figure 9a), orifice setting-c shrinks the work loop from left edge, indicating more resistance is introduced by the damper to reduce leg flexion. For the diaphragm damper (Figure 9b), orifice setting-c not only shrinks the work loop, but also increases its slope. We interpret this as the elastic contribution of air compression in the diaphragm damper: fewer air leaves through the smaller orifice.

Concerning energy dissipation, changes of orifice settings led to relatively small changes in effective dissipated energy $E_{\text{effective}}$: 150 mJ to 156 mJ for hydraulic damper, and 100 mJ to 102 mJ for diaphragm damper. Even for the other damper model (1210M), which dissipates high amounts of energy, changes in orifice setting change the work-loop shape drastically, but not the dissipated energy (395 mJ versus 401 mJ). Similar to the isolated damper drop, the data (Figure 9a, 9b) shows that specific orifice settings introduce more resistance, but not necessarily lead to higher energy dissipation, for both hydraulic and diaphragm damper. The non-linear coupling between damper and leg dynamics makes the prediction of the energy dissipation not straight-forward and points towards additional effects which are not considered in our simplified numerical leg model, according to which an increase in damping coefficients leads to a systematic increase of dissipated energy (Table 2).

Discussing insights from the here presented damper-spring leg-drop experiments, with respect to animal locomotion experiments is somewhat early. However, observations from (Müller et al., 2014, Table 1, page 2288) indicate that leg forces can increase at unexpected step-downs during locomotion experiments. Hence our results of adjustable, viscous dampers in parallel to elastic structures, acting as mechanically adaptive mechanisms, and producing additional forces but without the need for sensing, is exciting.

6 CONCLUSION

We investigated the possibility to exploit physical damping in a simplified leg drop scenario as a template for the early stance phase of legged locomotion. Our results from a) numerical simulation promote the use of adjustable and viscous damping over Coulomb damping to deal with a ground perturbation by physical damping. As such, we b) tested two technical solutions in hardware: a commercial, off-the-shelf hydraulic damper, and a custom-made, rolling diaphragm damper. We dissected the observed dissipated energy from the hardware damper-spring leg drops, into its components, by experimental design. The resulting data allowed us to characterize dissipation from the early impact (unsprung-mass effects), viscous damping, Coulomb damping, and orifice adjustments *individually, and qualitatively*. The rolling diaphragm damper features low-Coulomb friction, but dissipates only low amounts of energy through viscous damping. The off-the-shelf, leg-mounted hydraulic damper did exhibit high viscous damping, and qualitatively showed the expected relationship between impact speed, output force and negative work. Changes in orifice setting showed only minor changes in overall energy dissipation, but can lead to large changes in leg

length dynamics, depending on the chosen technical damper. Hence switching between different viscous, hydraulic dampers is an interesting future option. Our results show how viscous, hydraulic dampers react velocity dependent, and create an instantaneous, physically adaptive response to ground-level perturbations without sensory-input.

CONFLICT OF INTEREST STATEMENT

The authors declare that the research was conducted in the absence of any commercial or financial relationships that could be construed as a potential conflict of interest.

AUTHOR CONTRIBUTIONS

AM contributed to concept, hardware design, experimental setup, experimentation, data discussion and writing. FI contributed to concept, simulation framework, experimental setup, data discussion and writing. DH and ABS contributed to concept, data discussion and writing.

ACKNOWLEDGMENTS

The authors thank the International Max Planck Research School for Intelligent Systems (IMPRS-IS) for supporting AM, FI, the China Scholarship Council (CSC) for supporting AM, and the Ministry of Science, Research and the Arts Baden-Württemberg (Az: 33-7533.-30-20/7/2) for supporting DH, and the Max Planck Society for supporting ABS.

REFERENCES

- Abraham, I., Shen, Z., and Seipel, J. (2015). A Nonlinear Leg Damping Model for the Prediction of Running Forces and Stability. *Journal of Computational and Nonlinear Dynamics* 10. doi:10.1115/1.4028751
- Bledt, G., Wensing, P. M., Ingersoll, S., and Kim, S. (2018). Contact model fusion for event-based locomotion in unstructured terrains. In *2018 IEEE International Conference on Robotics and Automation (ICRA), Brisbane, Australia, Submitted (IEEE)*, 1–8
- Blickhan, R., Seyfarth, A., Geyer, H., Grimmer, S., Wagner, H., and Günther, M. (2007). Intelligence by mechanics. *Philosophical Transactions of the Royal Society of London, Series A* 365, 199–220. doi:10.1098/rsta.2006.1911
- Dixon, J. C. (2008). *The shock absorber handbook* (John Wiley & Sons)
- Garcia, E., Arevalo, J. C., Munoz, G., and Gonzalez-de Santos, P. (2011). Combining series elastic actuation and magneto-rheological damping for the control of agile locomotion. *Robotics and Autonomous Systems* 59, 827–839
- Ghazi-Zahedi, K., Haeufle, D. F. B., Montúfar, G., Schmitt, S., and Ay, N. (2016). Evaluating Morphological Computation in Muscle and DC-motor Driven Models of Human Hopping. *Frontiers in Robotics and AI* 3, 1–10. doi:10.3389/frobt.2016.00042
- Grimminger, F., Meduri, A., Khadiv, M., Viereck, J., Wüthrich, M., Naveau, M., et al. (2020). An Open Force-Controlled Modular Robot Architecture for Legged Locomotion Research. *The IEEE Robotics and Automation Letters (in press)*
- Haeufle, D. F. B., Grimmer, S., and Seyfarth, A. (2010). The role of intrinsic muscle properties for stable hopping - stability is achieved by the force-velocity relation. *Bioinspiration & Biomimetics* 5, 016004. doi:10.1088/1748-3182/5/1/016004

- Havoutis, I., Semini, C., Buchli, J., and Caldwell, D. G. (2013). Quadrupedal trotting with active compliance. In *Mechatronics (ICM), 2013 IEEE International Conference on* (IEEE), 610–616
- Hu, C.-J., Wang, T.-K., Huang, C.-K., and Lin, P.-C. (2019). A torque-actuated dissipative spring loaded inverted pendulum model with rolling contact and its application to hexapod running. *Bioinspiration & biomimetics* 14. doi:10.1088/1748-3190/aafc4e
- Hutter, M., Gehring, C., Bloesch, M., Hoepflinger, M. A., Remy, C. D., and Siegwart, R. (2012). Starleth: A compliant quadrupedal robot for fast, efficient, and versatile locomotion. In *Adaptive Mobile Robotics* (World Scientific), 483–490
- Hutter, M., Gehring, C., Jud, D., Lauber, A., Bellicoso, C. D., Tsounis, V., et al. (2016). Anymal - a highly mobile and dynamic quadrupedal robot. *2016 Ieee/Rsj International Conference on Intelligent Robots and Systems (Iros 2016)* , 38–44
- Josephson, R. K. (1985). Mechanical power output from striated muscle during cyclic contraction. *Journal of Experimental Biology* 114, 493–512
- Kalouche, S. (2017). Goat: A legged robot with 3d agility and virtual compliance. In *2017 IEEE/RSJ International Conference on Intelligent Robots and Systems (IROS)*. 4110–4117. doi:10.1109/IROS.2017.8206269
- Kalveram, K. T., Haeufle, D. F. B., Seyfarth, A., and Grimmer, S. (2012). Energy management that generates terrain following versus apex-preserving hopping in man and machine. *Biological Cybernetics* 106, 1–13. doi:10.1007/s00422-012-0476-8
- Mochon, S. and McMahon, T. A. (1980). Ballistic walking: An improved model. *Mathematical Biosciences* 52, 241–260
- More, H. L. and Donelan, J. M. (2018). Scaling of sensorimotor delays in terrestrial mammals. *Proc. R. Soc. B* 285, 20180613. doi:10.1098/rspb.2018.0613
- More, H. L., Hutchinson, J. R., Collins, D. F., Weber, D. J., Aung, S. K. H., and Donelan, J. M. (2010). Scaling of Sensorimotor Control in Terrestrial Mammals. *Proceedings of the Royal Society B: Biological Sciences* 277, 3563–3568. doi:10.1098/rspb.2010.0898
- Müller, R., Tschiesche, K., and Blickhan, R. (2014). Kinetic and kinematic adjustments during perturbed walking across visible and camouflaged drops in ground level. *Journal of Biomechanics* 47, 2286–2291. doi:10.1016/j.jbiomech.2014.04.041
- Rummel, J. and Seyfarth, A. (2008). Stable Running with Segmented Legs. *The International Journal of Robotics Research* doi:10.1177/0278364908095136
- Ruppert, F. and Badri-Spröwitz, A. (2019). Series Elastic Behavior of Biarticular Muscle-Tendon Structure in a Robotic Leg. *Frontiers in Neurorobotics* 13, 64. doi:10.3389/fnbot.2019.00064
- Secer, G. and Saranli, U. (2013). Control of monopodal running through tunable damping. In *2013 21st Signal Processing and Communications Applications Conference (SIU)* (IEEE), 1–4. doi:10.1109/SIU.2013.6531557
- Seok, S., Wang, A., Chuah, M. Y. M., Hyun, D. J., Lee, J., Otten, D. M., et al. (2015). Design principles for energy-efficient legged locomotion and implementation on the MIT cheetah robot. *IEEE/ASME Transactions on Mechatronics* 20, 1117–1129. doi:doi.org/10.1109/TMECH.2014.2339013
- Serafin, S. (2004). *The sound of friction: real time models, playability and musical applications*. Thesis, Department of Music
- Shen, Z. and Seipel, J. (2012). A fundamental mechanism of legged locomotion with hip torque and leg damping. *Bioinspiration & biomimetics* 7, 046010. doi:10.1088/1748-3182/7/4/046010

- Spröwitz, A., Tuleu, A., Vespignani, M., Ajallooeian, M., Badri, E., and Ijspeert, A. J. (2013). Towards dynamic trot gait locomotion: Design, control, and experiments with cheetah-cub, a compliant quadruped robot. *The International Journal of Robotics Research* 32, 932–950
- Whitney, J. P., Chen, T., Mars, J., and Hodgins, J. K. (2016). A hybrid hydrostatic transmission and human-safe haptic telepresence robot. In *Proceedings of ICRA (IEEE)*, 690–695
- Whitney, J. P., Glisson, M. F., Brockmeyer, E. L., and Hodgins, J. K. (2014). A low-friction passive fluid transmission and fluid-tendon soft actuator. In *Proceedings of IROS (IEEE)*, 2801–2808
- Zahedi, K. and Ay, N. (2013). Quantifying morphological computation. *Entropy* 15, 1887–1915. doi:10.3390/e15051887